Thermal conductivity of Fe-Si alloys and thermal stratification in

1

Earth's core 2 3 Youjun Zhang^{a,1}, Kai Luo^{b,c,1}, Minggiang Hou^{d,1}, Peter Driscoll^b, Nilesh P. Salke^e, Ján Minár^f, 4 Vitali B. Prakapenka^g, Eran Greenberg^{g,k}, Russell J. Hemley^{e,h,i}, R. E. Cohen^{b,2}, and Jung-Fu 5 Lin^{j,2} 6 7 ^aInstitute of Atomic and Molecular Physics, Sichuan University, Chengdu 610065, China; 8 9 ^bEarth and Planets Laboratory, Carnegie Institution for Science, 5251 Broad Branch Rd. NW, Washington, DC 20015, USA; 10 11 Department of Applied Physics, Nanjing University of Science and Technology, Nanjing, Jiangsu 12 210094, China: dState Key Laboratory of Geodesy and Earth's Dynamics, Innovation Academy for Precision 13 14 Measurement Science and Technology, Chinese Academy of Sciences, Wuhan 430077, China; ^eDepartment of Physics, University of Illinois Chicago, Chicago, IL 60607, USA; 15 ^fNew Technologies-Research Centre, University of West Bohemia, Univerzitní 8, 306 14 Plzeň, Czech 16 17 Republic; 18 ^gCenter for Advanced Radiation Sources, University of Chicago, Illinois 60637, USA; ^hDepartment of Chemistry, University of Illinois Chicago, Chicago, IL 60607, USA; 19 ¹Department of Earth and Environmental Sciences, University of Illinois Chicago, Chicago, IL 60607, 20 21 USA; Department of Geological Sciences, Jackson School of Geosciences, The University of Texas at Austin, 22 23 Austin, TX 78712, USA; 24 ^kCurrent affiliation: Applied Physics Division, Soreq Nuclear Research Center (NRC), Yavne 81800, 25 Israel. 26 ¹Y.Z., K.L., and M.H. contributed equally to this work. 27 28 ²To whom correspondence should be addressed. Email: rhemley@uic.edu, rcohen@carnegiescience.edu, 29 afu@jsg.utexas.edu 30 31

Abstract

Light elements in Earth's core play a key role in driving convection and influencing geodynamics, both of which are crucial to the geodynamo. However, the thermal transport properties of iron alloys at high pressure-temperature conditions remain uncertain. Here we investigate the transport properties of solid hcp and liquid Fe-Si alloys with 4.3 and 9.0 wt.% Si at high pressure-temperature using laser-heated diamond anvil cell experiments and first-principles molecular dynamics and dynamical mean field theory calculations. In contrast to the case of iron, silicon impurity scattering gradually dominates the total scattering in Fe-Si alloys with increasing Si concentration, leading to temperature-independence of the resistivity and less electron-electron contribution to the conductivity in Fe-9Si. Our results show a thermal conductivity of \sim 100-110 W m⁻¹K⁻¹ for liquid Fe-9Si near the topmost outer core. If Earth's core consists of a high amount of silicon (e.g., > 4.3 wt.%) with such a high thermal conductivity, a subadiabatic heat flow across the core-mantle boundary is likely, leaving a 400-500-km-deep thermally stratified layer below the CMB and challenges proposed thermal convection in Fe-Si liquid outer core.

- **Keywords**: thermal conductivity, Earth's core, geodynamo, light elements
- 49 Classifications: physical sciences

Significance (< 120 words)

Earth's liquid outer core is mainly composed of iron alloyed with ~8-10% of light elements (e.g., silicon). Convection of the liquid core generates Earth's magnetic field, which is controlled by the thermal conductivity of the core. In this study, we investigated the resistivity and thermal conductivity of iron-silicon alloys as a candidate composition in Earth's core via high pressure-temperature experiments and numerical calculations. We found a nearly temperature-independence of the resistivity in iron-silicon alloys at Earth core's pressure and thus a high thermal conductivity. This work indicates that if silicon is the sole major light element in Earth's core, it could depress thermal convection and promote a thermally stratified layer at the topmost outer core.

Introduction

61

62

63

64

65

66

67

68

69

70

71

72

73

74

75

76

77

78

79

80

81

82

83

84

85

86

87

88

89

90

91

The geodynamo of Earth's core is thought to be mainly driven by compositional (chemical) convection associated with the crystallization and light element release of the inner core as well as thermal convection driven by a superadiabatic heat flow across the core-mantle boundary (CMB). The relative importance of these energy sources to the geodynamo, however, remain uncertain (1). The magnitudes of these energy sources can change throughout the evolution of the planet. The thermal gradient across the CMB can be constrained from both heat flow of the core and mantle, where a subadiabatic heat flow out of the core may hinder thermal convection and cause a thermally stratified layer at the top of the outer core (2). A global non-adiabatic structure at the top of the core has been inferred from seismic observations and geomagnetic fluctuations (3, 4), where the mechanisms for the origin rely on accurate determinations of the CMB heat flow and the core conductivity. Based on seismological observations and high pressure-temperature (P-T) mineral physics results, Earth's outer and inner core are mainly composed of Fe (~85 wt.%) alloyed with Ni (~5 wt.%) and approximately 8-10 wt.% and 4-5 wt.% of light elements, respectively, such as Si, O, S, C, and H (5-10). The effects of the candidate light elements on the electrical resistivity (ρ_e) and thermal (κ) conductivities of iron and their partitioning between the inner and outer core at relevant P-T conditions are thus of great importance for understanding the thermal state of the core as well as the generation and evolution of Earth's magnetic field (2, 9, 11, 12). The thermal conductivity of the constituent core alloy controls the heat flow of the core while the electrical resistivity of the constituent Fe alloy determines the ohmic dissipation rate of the magnetic field.

Extensive studies on iron's transport properties have been conducted via experiments and calculations (*e.g.*, (13-21)), and recent studies report a thermal conductivity of ~100 W m⁻¹ K⁻¹ at conditions near the CMB (22, 23). Such a high thermal conductivity reduces the amount of heat that can be transported by convective flow (11) and raises a question as to what powered the convection prior to inner core growth over Earth's history (the so-called new core paradox (24)). Thus far, several hypotheses have been proposed to reconcile this paradox, including a possible large conductivity reduction due to nickel and light elements (25-28), a rapid core cooling rate (29), or exsolution of chemically saturated species from the core to the lowermost mantle, such as MgO, SiO₂, or FeO (*e.g.*, (30-32)). The general consensus is that incorporation of light element(s) depresses high P-T thermal conductivity of iron by impurity scattering (12). The

lowered thermal conductivity would consequently lead to stronger thermal convection being inferred in the core. The rapid core cooling model would imply a young inner core and requires a hidden core heat source, such as radioactivity, which is not supported by geochemical evidence (29). The exsolution mechanism would offer an additional energy source to drive an early compositionally-driven geodynamo (32), although some experiments find exsolution to be unlikely (33). The viability of each of these scenarios depends sensitively on the transport properties of iron alloyed with a significant amount of light element(s) (approximately 8-10 wt.%) at core *P-T* conditions. Information on these electrical and thermal transport properties of iron alloys remain uncertain due to the sparsity of experimental and theoretical data.

Here we focus on the geodynamic consequences of the transport properties of iron alloyed with 4-10 wt.% silicon, which is considered to be one of the major light element candidates in the Earth's core due to its geo- and cosmo-chemical abundance (5), high solubility in solid and liquid iron (34), and isotopic evidence (35). Fe-Si alloys have been the subject of previous studies focused on understanding the structural and physical properties of the core material, including its high P-T phase diagram (36-39), elasticity (40-44), melting behavior (36, 45, 46), and transport properties (25, 47-49). The observed density discontinuity of ~4–5% across the inner-core boundary (ICB) indicates that excess light elements partition into the outer core during inner-core solidification (6, 50). We should note that the concentration of Si in the core remains uncertain. While some experiments have shown that Fe alloyed with ~9 wt.% Si can satisfy the density profile of the outer core and Fe alloyed with ~4 wt.% Si for the inner core, respectively (37, 40, 41, 53, 54), other studies indicate that a dominant Si light alloying component is unable to reproduce both the density and sound velocity distribution in the outer core (51, 52).

High P-T diamond anvil cell (DAC) experiments had been previously conducted to constrain the electrical and thermal conductivity of Fe-Si alloys (28, 47, 55, 56), specifically their T-dependent resistivity and thermal conductivity at core pressures. The thermal conductivity of Fe-8wt.%Si (hereafter Fe-8Si) was measured using a high-P ultrafast optical pump-probe and high P-T flash heating methods (28). The results showed that 8 wt.% silicon in solid hcp Fe can strongly reduce the conductivity of pure iron by a factor of ~2, i.e., giving ~20 W m⁻¹ K⁻¹ at ~132 GPa and 3000 K. However, the electrical resistivity of solid Fe-6.5Si at ~99 GPa and 2000 K was recently measured to be ~73 $\mu\Omega$ cm (56), which is higher than that of pure

iron (22) by ~60% at comparable conditions. The results imply a thermal conductivity of ~66 W m⁻¹ K⁻¹ using the Wiedemann-Franz law ($TL = \rho_e \kappa$) assuming an ideal Sommerfeld Lorenz number ($L=L_0$: 2.44×10⁻⁸ W m⁻¹ K⁻²). Meanwhile, another recent study reported a moderate thermal conductivity of 50-70 W m⁻¹ K⁻¹ for an Fe-5Ni-8Si alloy near CMB P-T conditions (~140 GPa and 4000 K) modeled from the measured resistivity of Fe-10Ni and Fe-1.8Si alloys using the four-probe van der Pauw method in laser-heated DACs (25). The results on Fe-10Ni and Fe-1.8Si alloys reveal a linear relationship between resistivity and temperature at a given high pressure, which is very similar to that of hcp Fe (22), over the range of measurements. In contrast, density functional theory-based molecular dynamics (DFT-MD) simulations predict a small negative T-dependence of the resistivity at high pressure when liquid Fe is alloyed with a significant amount of light elements (e.g., ~13 wt.% Si) (27). These experimental and computational results raise the possibility that the high P-T thermal transport behavior and its temperature dependence in Fe-Si alloys with a few wt.% Si (e.g., 2 wt.%) and a larger wt.% Si (e.g., 8-10 wt.%) can be quite different, making it difficult to evaluate the light element effects on the energetics of the core.

In this study, we directly measured the electrical resistivities of polycrystalline hcp Fe-4.3wt.%Si (Fe-4.3Si, or Fe_{0.92}Si_{0.08}) and Fe-9wt.%Si (Fe-9Si, or Fe_{0.84}Si_{0.16}) alloys to ~136 GPa and 3000 K. We also computed the electrical resistivity and thermal conductivity of these Fe-Si alloys in solid and liquid phases using first-principles molecular dynamics (FPMD) and dynamical mean field theory (DMFT) calculations. The calculations include contributions from scattering off of Si as well as both electron-phonon (e-ph) and electron-electron (e-e) scattering. Our results are used to evaluate the Si impurity effects on the transport properties of Fe-Si alloy at *P-T* conditions of the topmost outer core. Assuming Si is the sole light element in the core, our results are used to constrain core thermal conductivity which is in turn used to assess core heat flux, thermal state, and energy sources driving the geodynamo through geodynamical modeling.

F

Results

The electrical resistivity of polycrystalline Fe-4.3Si and Fe-9Si alloys was measured in flattop laser-heated DACs using the four-probe van der Pauw method (see Methods and SI Appendix, Figs. S1 and S2). Initial measurements of Fe-9Si up to ~136 GPa at room temperature (SI Appendix, Fig. S3) are consistent with previous studies on Fe-Si alloys up to ~90 GPa (47,

55). The well-known bcc-hcp (α - ϵ) phase transition observed at ~15 GPa causes an increase in the resistivity (SI Appendix, Fig. S3). With further increase in pressure, the resistivity of hcp Fe-9Si gradually diminishes and the pressure coefficient of resistivity decreases. The hcp-structured Fe-Si alloys have higher resistivities than pure hcp Fe due to the impurity scattering. We find that the resistivity in the Fe-Si alloys increases quasilinearly with increasing silicon concentration up to ~9.0 wt.% at room temperature (47).

At ~100, 120, and 136 GPa, electrical resistivities of the polycrystalline Fe-Si alloys were measured with increasing temperature up to ~3000 K (Figs. 1-2 and SI Appendix, Fig. S4). Insitu powder x-ray diffraction (XRD) patterns of the samples show well-distributed intensity, indicating that the polycrystalline samples in the hcp structure did not experience significant lattice-preferred orientation due to possible deviatoric stresses and/or high temperature-induced recrystallization over the investigated P-T conditions (SI Appendix, Figs. S4-S5). The use of strong cubic boron nitride (cBN) as the gasket insert and two flat layers of SiO₂ as the pressure medium in our experiments provided that the samples maintained their initial crossed-heart shapes and even thicknesses that are critical for the success of the four-probe van der Pauw method. The laser heating experiments were conducted up to approximately 2500-3000 K, which is below the expected fast-recrystallization threshold needed to avoid the possible influence of recrystallization on conductivity (SI Appendix, Fig. S4) (57, 58). The hcp phase was observed in Fe-4.3Si and Fe-9Si alloys at these high *P-T* conditions, consistent with the previously determined stability field of the hcp phase (SI Appendix, Text S1 and Figs. S4-S5) (59). Analysis of the quenched Fe-9Si samples after the high P-T measurements showed compositional homogeneity of Fe with 9.6(1.8) wt.% Si (see Methods). These results indicate that the samples were not chemically contaminated and the hcp Fe-9Si alloy was the predominant phase during the high *P-T* measurements (SI Appendix, Text S1, Table S1, and Fig. S6).

Our results show that the resistivity of hcp Fe-4.3Si alloy increases linearly with increasing temperature at high pressures over the measured range (SI Appendix, Figs. 1-2). However, the resistivity-temperature slope in hcp Fe-4.3Si is significantly lower than that of literature values for hcp Fe and Fe-1.8Si alloy (22, 25). Our measured resistivity of hcp Fe-4.3Si is also consistent with the previous results using a four-probe method in an internally heated DAC, where it is located between those of hcp Fe-4Si and Fe-6.5Si up to \sim 3000 K at \sim 100 GPa (56) (Fig. 1). For

simplicity, we used the Bloch-Grüneisen formula to fit the measured resistivity data (SI Appendix, Table S2):

186
$$\rho_{e-Fe-Si}(V,T) = \rho_{e-r} + \rho_{e-BG}(V,T) = \rho_{e-r} + D_{\rho}(V) \left(\frac{T}{\theta_{D}(V)}\right)^{n} \int_{0}^{\theta_{D}(V)/T} \left[\frac{z^{n}}{(e^{z}-1)(1-e^{-z})}\right] dz$$
 [1]

where ρ_{e-r} is the residual electrical resistivity of Fe-Si alloys when the phonons of the alloys are frozen, and ρ_{e-r} , n, and $D_{\rho}(V)$ are fitted constants based on the measured resistivities at high P-T. Fitting results show a weakening temperature dependence of the resistivity in hcp Fe-Si alloys with increasing concentrations of silicon. The fitted n parameter in the Bloch-Grüneisen formula that describes the T-dependence of the resistivity decreases from 1-3 in hcp Fe (22) to 0.6-0.7 in hcp Fe-1.8Si (25), then down to 0.15-0.18 in hcp Fe-4.3Si at similar P-T conditions (SI Appendix, Table S2). Furthermore, the resistivity of the Fe-9Si alloy appears to be nearly constant with increasing temperature (Fig. 1). For example, the resistivity of hcp Fe-9Si varies from 81(3) $\mu\Omega$ cm at room temperature to 84(4) $\mu\Omega$ cm at 2120(90) K at ~100 GPa, so there is no visible temperature effect on the resistivity within uncertainties. As a result, the Bloch-Grüneisen n parameter is close to 0 in hcp Fe-9Si (Fig. 1; SI Appendix, Table S2). Note that the Bloch-Grüneisen formula is derived only for e-ph scattering, so it is not surprising that the fitted n parameters are anomalous for Fe-Si alloys where impurity scattering dominates. At relatively low temperatures, the resistivity of hcp Fe is much lower than those of Fe-Si alloys due to the impurity scattering; however, they approach each other with increasing temperature due to the lower temperature coefficient of resistivity in the hcp Fe-4.3Si and Fe-9Si alloys (Fig. 1).

We computed the electrical resistivity of the hcp Fe-Si alloys at P-T conditions similar to those in the present experiments using FPMD/DFT/DMFT calculations that include e-ph, chemical impurity, and e-e scatterings (See Methods). Overall, the calculated high P-T resistivities of hcp Fe-4.3Si and Fe-9Si alloys are consistent with our experimental results (open red and blue diamonds for Fe-4.3Si and Fe-9Si, respectively, Figs. 1-2). These calculations do not assume Matthiessen's rule (that scattering is additive) or the Wiedemann-Franz law. Both experiments and theory consistently show that the T-dependence of the resistivity decreases with increasing the concentration of silicon. The calculated resistivity of hcp Fe-Si alloys is also compared with the FPMD/DFT calculations including only e-ph and impurity scattering (semi-open diamonds in Figs. 1-2). The results show that the e-e contribution to the resistivity of hcp Fe-4.3Si and Fe-9Si alloys is less than $\sim 10\%$ at high temperatures and pressures of 90-140 GPa

(Figs. 1-2). Specifically, the e-e contribution increases with increasing temperature but it 214 decreases with increasing Si concentration in hcp Fe-Si alloys at high pressures (SI Appendix, 215 216 Fig. S7). For example, the e-e contribution in hcp Fe-9Si could be less than ~6% near the CMB conditions (~4000 K and 136 GPa, Fig. 2), in contrast to the significant contribution to hep iron 217 where it is $\sim 30\%$ (SI Appendix, Fig. S7). 218 219 Our theoretical results indicate that impurity scattering is the main contribution to the high P-T resistivity of Si-doped Fe alloys (4.3-9.0 wt.%Si) (Figs. 1-2). The resistivities of hcp Fe and 220 Fe-Si alloys with low Si concentrations such as Fe-1.8Si exhibit a significant T-dependence (22, 221 23, 25) because the e-ph and e-e scattering from iron then dominates the total scattering and is T-222 dependent. With increasing Si concentration in Fe-Si alloys, the T-independent Si impurity 223 scattering gradually takes over the total scattering, leading to T-independence and less e-e 224 contribution in the resistivity of Fe-9Si (Figs. 1-2). The low T-dependence in the resistivity of 225 Fe-Si alloys was predicted and previously explained by the chemically-induced "resistivity 226 saturation" in some early DFT studies (47). However, the effect documented here is not 227 resistivity saturation, but rather is due to the impurity scattering being nearly T-independent and 228 229 dominant, as well as a breakdown of Matthiessen's rule. The electrical resistivity and thermal conductivity of hcp and molten Fe-Si alloys at P-T 230 231 conditions relevant to the core were further calculated using DFT/DMFT (Fig. 3). We assumed that the Fe-Si alloys remain in the hcp phase near CMB pressure below ~4000 K and are molten 232 233 above 6000 K, consistent with the determined melting relation of Fe-Si alloys (36, 38, 45). Based on our experimental and theoretical results, the resistivity of hcp Fe-4.3Si and Fe-9Si is 234 235 estimated to be 80(6) and 90(6) $\mu\Omega$ ·cm at 140 GPa and 4000 K, respectively (Fig. 3a). The computations also predict that the resistivity of Fe-Si alloys does not significantly change upon 236 237 melting above 6000 K (Fig. 3a and SI Appendix, Fig. S8). The minor effect of melting can be 238 understood as a result of the dominant electronic contribution on the resistivity in both hcp Fe and liquid phase, and the fact that under high compression the local structures of liquid and solid 239 are similar. The thermal conductivity of hcp Fe-Si alloys was then determined from both the 240 calculations and the measured resistivity via the Wiedemann-Franz law using our computed 241 242 Lorenz number. The calculated Lorenz number (L) varies with temperature at the pressure of the topmost core (Fig. 3c). At P-T conditions of the CMB (135-150 GPa and ~4000 K), the 243 calculated Lorenz number of hcp Fe-Si alloys (2.33-2.39×10⁻⁸ W Ω K⁻²) does not deviate 244

appreciably from the Sommerfeld value L_0 (2.44×10⁻⁸ W m⁻¹K⁻²), but they are significantly larger than that of hcp Fe (2.1×10⁻⁸ W Ω K⁻²) (22). Our results show that the thermal conductivity of hcp and liquid Fe-Si alloys increases linearly with increasing temperature at the pressure near the CMB (Fig. 3b). Further, the theoretical results predict little change on the melting due to electronic contribution being dominant in liquid iron which has a local atomic structure similar to the hexagonal close-packed structure (60).

The thermal conductivity of hcp Fe-9Si is found to be $\sim 100\text{-}110~\text{W}$ m⁻¹ K⁻¹ at $\sim 140~\text{GPa}$ and 4000~K based on both experimental and theoretical results, which is unexpectedly close to that of pure hcp Fe at similar conditions ($100\pm 10~\text{W}$ m⁻¹ K⁻¹) (22). Therefore, adding 9 wt.% Si into iron does not reduce its thermal conductivity near CMB conditions. Surprisingly, the thermal conductivity of hcp/liquid Fe-9Si alloy is likely larger than that of Fe with further increasing temperature above 4000~K (Fig. 3b). The incorporation of a large amount of Si (*e.g.*, 9 wt.%) in Fe makes Fe-Si alloy an even better thermal conductor at very high temperatures because the thermal conductivity continuously increases but resistivity is almost constant with increasing temperature. Although we did not consider the phonon contribution to the thermal conductivity of Fe-Si alloys, it has been previously evaluated to be $\sim 3~\text{W}$ m⁻¹K⁻¹ in Fe alloy (61). The result indicated a negligible contribution from phonons compared to the electronic contribution of 100-110 W m⁻¹ K⁻¹ in Fe-Si alloys.

Compared with the recently modeled thermal conductivity of Fe-Si alloys obtained from high P-T measurements of heat pulse propagation in samples in laser-heated DACs (28), our estimated thermal conductivity of Fe-(4.3-9.0)Si alloy (~78 W m⁻¹ K⁻¹) at 120-140 GPa and ~2500 K are slightly higher than that of Fe-2Si (~64±16 W m⁻¹ K⁻¹, inverted triangle, Fig. 3b), but ~4 times larger than that of Fe-8Si alloys (~20±10 W m⁻¹ K⁻¹, triangle, Fig. 3b) from the previous experiments (Fig. 3b). The large discrepancy of high P-T thermal conductivity in Fe-8Si alloy obtained from the transient heating laser technique may arise from the large temperature uncertainty in the latter, leading to an indistinguishable temperature effect on the thermal conductivity in Fe-8Si (62). Another possibility is that Fe-8Si underwent a phase transition from hcp to mixed hcp with Si enriched bcc in the experiments of Ref. (28) because of higher temperatures (e.g., up to ~3800 K), where the hcp-bcc mixed-phase has lower thermal conductivity because of the lower conductivity in the bcc phase. Since our calculations predict a negligible effect of melting on these transport properties of Fe-Si alloys, our determined

resistivity and thermal conductivity of liquid Fe-4.3Si and Fe-9Si alloys at the *P-T* conditions of the outer core are also generally consistent with those of liquid Fe-6.7Si previously predicted using DFT techniques (Fig. 3b and SI Appendix, Fig. S10) (14, 27). Altogether, the results indicate that the e-ph and e-e scattering contribute less than the Si impurity scattering to the transport properties in these high P-T Fe-Si alloys.

Discussion

The experimental and theoretical results described above have important geodynamic implications. Although some distributions of other light elements are present in the core, we assume Si is dominant for purposes of the analysis (35). The high thermal conductivity of ~100-110 W m⁻¹ K⁻¹ of the Fe-9Si alloy at P-T conditions corresponding to the top of the liquid core (κ_c) indicates an adiabatic heat flow of ~15 TW ($Q_a = 4\pi r_{oc}^2 \kappa_{oc} \frac{\partial T}{\partial r}$, r_{oc} is the diameter of the outer core surface), assuming the temperature gradient ($\frac{\partial T}{\partial r}$) as ~0.9-1.0 K/km at the top of the outer core (11, 63). The present-day CMB heat flow across the lowermost mantle (Q_{cmb}) is constrained to be ~10-12 TW based on the estimated thermal conductivity (~10 W m⁻¹ K⁻¹) of the mantle minerals and temperature gradient in the lowermost mantle (64, 65). Thus, if ~9.0 wt.% Si is the sole light element concentration in the core, the adiabatic heat conduction limit of the core (Q_a) is most likely higher than Q_{cmb} and implies a subadiabatic temperature gradient in the core, thus inhibiting thermal convection.

The geodynamo is maintained by fluid convection in the outer core (66). It is believed that the fluid convection is mainly driven by thermal and/or compositional buoyancy, where the former requires a higher Q_{cmb} than the Q_a based on the Schwarzschild criterion (67), and the latter occurs with light element release from inner-core solidification (68). The high thermal conductivity in liquid Fe-9Si makes the core $Q_a > Q_{cmb}$ and thus hinders thermal convection. However, chemical buoyancy released at the ICB by inner core growth could still drive convection at depth. As a result, the present-day geodynamo would be mainly driven by compositional convection associated with the release of incompatible light elements and latent heat upon inner-core solidification (Fig. 4). Additionally, the present study shows a linearly increasing thermal conductivity in Fe-9Si alloy with temperature, which causes Q_a increased at

higher temperatures. Therefore, the early hotter liquid core had a higher thermal conductivity, making it even harder to drive a thermal dynamo.

Our results indicate that the uppermost core is sub-adiabatic and stable to thermal convection (11), which may result in thermal stratification at the top of the core unless the present-day Q_{cmb} is underestimated (Fig. 4). As a result, convection may be thermally stratified below the CMB and convectively unstable above the ICB in the core, with a transition radius r_s , or the thickness $z_s = R_c - r_s$ (R_c is the radius of the core) that we refer to as the depth of a thermally stratified layer (see Methods). To examine this effect of the thermal stratification in the outer core, we characterize the thermal inversion by investigating the Brunt-Väisälä frequency (N) (see Methods and SI Appendix, Text S3) and modeling the light element concentration perturbation, composition buoyancy, and total thermal and compositional buoyancy as a function of the radius (SI Appendix, Fig. S11 and Table S4). Convection occurs where the Brunt-Väisälä buoyancy frequency N is imaginary, where the N is defined by

$$N = \sqrt{-\frac{g}{\rho} \frac{d\rho}{dr}}$$
 [2]

g is the gravity, ρ is the density, and r is the radius, and $d\rho/dr$ is the radial derivation (3). Therefore, N=0 corresponds to the location of a transition from a convective to non-convective region. In the model, the computed thermal and compositional buoyancy profiles depend on Q_{cmb} and the total buoyancy gradient crosses zero at the stratification radius r_s (SI Appendix, Fig. S11). The thickness of the stratified layer (z_s) is then computed as a function of the Q_{cmb} assuming our determined Q_a of ~15 TW (see Methods) (Fig. 4a). Taking the Q_{cmb} of ~12 TW (64, 65), the thickness of the stratified layer is constrained to be ~400-500 km. The estimated thermal stratification layer overall overlaps the regions of the observed seismological velocity gradient at the top 100-700 km of the outer core from SmKS ($2 \le m \le 4$) analyses (4, 69, 70) (Fig. 4), but a recent seismic model requires no such an anomalous layer (71). We should also note that the thickness of the thermal stratification layer may show regional heterogeneity due to the proposed CMB heat flux variations (72). Further, the thermal stratification combined with possible chemical stratification likely causes the slight reduction of the seismic velocity atop Earth's outer core (73, 74).

and H can be incorporated into iron in its interstitial position. Hydrogen has long been considered as a light element (8), and in only small concentrations can have a significant effect on the core's properties (75). Recent studies indicate the presence of the other light elements chemically limit the H abundance (76). Different alloying may cause different temperature responses of the resistivity at high pressure according to a recent prediction (27), so electrical and thermal conductivity for other Fe-light element alloys at high P-T conditions need to be further evaluated by both experiments and theories. On the other hand, silicon is readily soluble in both solid and liquid iron at core P-T conditions (46). Thus, some other (multiple) light elements with different partitioning behaviors across the inner-core boundary (e.g., O and C (77, 78)) likely coexist in the core, which may partition between liquid and solid inner core to compositionally drive convection. Evidence for the presence of the geomagnetic field goes back to at least ~3.5 Ga (79), which may predate inner-core nucleation. This observation suggests that an Fe-9Si-rich core may have prevented an early thermal geodynamo before inner-core nucleation, raising again the core paradox (24). We therefore suggest that Si may not be the sole light element alloyed with iron in the core considering the negligible effect of Ni on the conductivity of iron (25), and a significant amount of other light elements discussed may co-exist in the liquid outer core. These light elements may have precipitated from the early molten core and accumulated in the lowermost mantle with the cooling of the core, consistent with a recent simulation indicates that 1-2 wt.% light element or oxide precipitation may have been sufficient to power the early dynamo (32). Future studies on the effects of all candidate light elements on the thermal transport properties of Fe-Ni alloy as well as Q_a and Q_{cmb} values at relevant high P-T conditions are critically needed to reliably evaluate the possible occurrence and thickness of the thermal stratification layer at the top of the outer core. In summary, we have performed electrical resistivity measurements coupled with in situ x-

335

336

337

338

339

340

341

342

343

344

345

346

347

348

349

350

351

352

353

354

355

356

357

358

359

360

361

362

363

364

365

In summary, we have performed electrical resistivity measurements coupled with *in situ* x-ray diffraction of Fe-Si alloys with 4.3-9.0 wt.% Si up to ~140 GPa and 3000 K in laser-heated DACs. The temperature-dependent resistivity of Fe-Si alloys has been determined by experiments and first-principles simulations. The overall consistent agreement between experiments and theory shows a greatly decreasing temperature coefficient of resistivity in Fe-Si alloys with increasing Si concentration. Electron-phonon scattering and impurity scattering dominate the contributions to the resistivity of the Fe-Si alloys whereas electron-electron scattering is much weaker (e.g., compared to pure iron). The thermal conductivity of liquid Fe-

9Si is constrained to be \sim 100-110 W m⁻¹ K⁻¹ near core-mantle boundary conditions. Such a high thermal conductivity hinders thermal convection and requires compositional convection in an FeSi core. The present study assuming Si as the major light element of the core indicates thermal stratification of the outer core with a \sim 400-500 km stagnant layer at the top of the core arising from subadiabatic heat flow across the core-mantle boundary. Further studies of the transport properties in other Fe alloys (*e.g.*, Fe-O/S/C/H and ternary Fe-Si-O/S/C/H alloys, etc.) at core *P*-T conditions could shed new light on the mechanism of the core convection over the Earth's history.

373374

375

376

377378

379

380

381 382

383

384

385

386 387

388

389

390

391

392

393

394 395

396

397398

366

367

368

369

370

371

372

Materials and Methods

Starting materials. Polycrystalline Fe-4.3Si and Fe-9Si alloys with bcc phase were used as starting materials. Fe-9Si alloy was the same one used in the previous study (39), which was purchased from Goodfellow Corporation. Fe-4.3Si was synthesized from a mixture of powder iron and silicon with a starting mass ratio of 95.7 and 4.3 by an arc-melting method in an arc furnace full of pure argon atmosphere to avoid any oxidation (43). The synthesized Fe-4.3Si sample was characterized by an electron probe microanalyzer (Shimadzu, EPMA-1720H) at Sichuan University, China. The backscattered electron image and EPMA analyses show a chemically homogenous composition in Fe-4.3Si alloy (SI Appendix, Fig. S1 and Table S3). The samples were compressed to thin foils with a thickness of 1.5–2 µm using a pair of diamond anvils with 600 µm culet diameter. The polycrystalline foils were shaped into a uniform Greek cross shape with a diameter of ~6 µm at the center (SI Appendix, Fig. S2a) by a Focused Ion Beam (FEI Versa 3D) at the Center of High-Pressure Science and Technology Advanced Research, Shanghai, China. The detailed process can be found in previous literature (22). The samples were loaded in DACs with 100-300 µm beveled culets with a beveled angle of 9 degrees and sandwiched between two dried SiO₂ layers (SI Appendix, Fig. S2a). We compressed the sample to targeted pressures in DACs and heated it using a flat-top double-sided laser heating system (SI Appendix, Fig. S2b). High P-T electrical resistivity measurements. High P-T electrical resistivity measurements on Fe-Si alloys and simultaneously in situ XRD in each run, were performed at the 13-IDD beamline station, GeoSoilEnviroConsortium for Advanced Radiation Sources (GSECARS) of the Advanced Photon Source (APS). The resistivity of Fe-4.3Si and Fe-9Si alloys were measured by a van der Pauw method using a Multimeter source (Keithley 6221 model) and an ultra-low voltmeter (Keithley 2182A model) at high pressures from ~90 to 136 GPa and temperatures up to ~3000 K, where their high P-T phase diagrams

have been well determined by previous laser-heated DAC experiments (38, 39, 59) (SI Appendix, Fig.

399 S4). The voltage was measured between electrical leads C and D and between A and D when a constant 400 direct current of 10 mA passed through the sample from electrical leads A to B and from B to C, 401 respectively. The resistance (R) at high P-T was calculated by Ohm's law according to the averaged voltage. In situ x-ray diffraction was collected along with the resistivity measurements of Fe-Si alloys 402 403 before, during, and after laser-heating by a Pilatus 1M CdTe detector at GSECARS. The resistivity was obtained from the equation of $\rho_e = \rho_{e0}(R/R_0)(V/V_0)^{1/3}$ (ρ_{e0} : the resistivity at room temperature and high P) 404 when taking into account the change of volume and assuming an isotropic deformation in the sample at 405 high P-T. Where, R_{θ} and V_{θ} are the resistance and volume at high pressure and room temperature, and R 406 407 and V are the measured resistance and voltage at high P-T conditions (SI Appendix, Fig. S4). The 408 pressure was obtained from the measured lattice parameters in Fe-Si alloys by in situ XRD, which were compared with the previously determined equation of states in Fe-4Si (59) and Fe-9Si (37, 39) alloys, 409 410 respectively. The chemical composition of the quenched Fe-Si samples was analyzed using a Scanning Electron Microscopy/Energy Dispersive X-ray Spectroscopy (SEM/EDS) (SI Appendix, Fig. S6 and 411 412 Table S1). 413 Computation details for electrical and thermal transport properties. First-principles molecular 414 dynamics (FPMD) simulations for Fe-Si were performed using QUANTUM ESPRESSO (80). All the 415 FPMD calculations used the ground-state Perdew-Burke-Ernzerhof (PBE) (81) generalized gradient 416 approximation for the exchange-correlation functional. Supercells containing 216 atoms in the hcp 417 structure were prepared for random placement of the Si atoms in the hcp lattice with the tool Alloy 418 Theoretic Automated Toolkit (ATAT) using the Special Quasi-random Structures (SQS) algorithm (82, 419 83). The lattice constants from the XRD measurements in this study were used. We used scalar-420 relativistic Garrity-Bennett-Rabe-Vanderbilt (GBRV) ultrasoft pseudopotentials for Fe and Si, which 421 were generated using smaller cutoff radii. The pseudopotentials were tested against linearized augmented plane wave (LAPW) (84) and standard GBRV pseudopotentials. The plane-wave cutoff energy was 40 422 423 Ry. For each temperature, the ionic temperature was regulated by the stochastic-velocity rescaling thermostat (85) in the N-V-T ensemble and identical electronic temperatures were set with the Fermi-424 425 Dirac smearing function. The Brillouin zone is sampled at the Γ -point in the FPMD. The FPMD step was 426 1 fs and the simulations were longer than 10 ps to ensure the equilibrium state was reached. All bands 427 with occupations larger than 10⁻⁵ were included. Macroscopic quantities, such as temperature and 428 pressure, were obtained by averaging over 3000 or more equilibrium steps. 429 In the transport calculations of Fe-Si alloys, we employed relativistic KKR-DMFT as implemented in a modified Spin-polarized Relativistic KKR (SPRKKR) package (86, 87) to selected snapshots. These 430 431 snapshots were separated from each other by more than the velocity correlation time under each 432 condition. For each one, the calculations were separated into 3 steps: (i) DFT self-consistent-field (SCF)

- calculation; (ii) SCF calculation at the DMFT level; and (iii) transport calculations with potentials from
- 434 (i) and (ii) using Kubo-Greenwood method (see SI Appendix, eqs. [S1]-[S4]) (88, 89). The converged
- potential of selected ionic configurations was then used as the starting potential for the next step.
- 436 Additional details are presented in the Supporting Information (SI Appendix, Text S2).

437438

REFERENCES:

- 1. C. A. Jones, "Thermal and Compositional Convection in the Outer Core" in Treatise on Geophysics (Second Edition), G. Schubert, Ed. (Elsevier, Oxford, 2015), vol. 8, pp. 115-159.
- 441 2. F. Nimmo, "Energetics of the Core" in Treatise on Geophysics (Second Edition), G. Schubert, Ed. (Elsevier, Oxford, 2015), vol. 8, pp. 27-55.
- 3. B. Buffett, Geomagnetic fluctuations reveal stable stratification at the top of the Earth's core.

 Nature **507**, 484-487 (2014).
- 4. G. Helffrich, S. Kaneshima, Outer-core compositional stratification from observed core wave speed profiles. *Nature* **468**, 807-810 (2010).
- J. Li, Y. Fei, "Experimental constraints on core composition" in Treat. Geochem., K. K.
 Turekian, Ed. (Elsevier, Oxford, 2014), pp. 527-557.
- W. F. McDonough, "Compositional model for the Earth's core" in Treat. Geochem., R. W. Carlson, H. Holland, K. Turekian, Eds. (Elsevier, Amsterdam, 2014), vol. 3, pp. 559-577.
- 451 7. Y. Fei, C. Murphy, Y. Shibazaki, A. Shahar, H. Huang, Thermal equation of state of *hcp*-iron:
 452 Constraint on the density deficit of Earth's solid inner core. *Geophys. Res. Lett.* **43**, 6837-6843
 453 (2016).
- 454 8. Q. Williams, R. J. Hemley, Hydrogen in the Deep Earth. *Annu. Rev. Earth Planet. Sci.* **29**, 365-418 (2001).
- 456 9. R. J. Hemley, H.-K. Mao, In Situ Studies of Iron under Pressure: New Windows on the Earth's Core. *Int. Geol. Rev.* **43**, 1-30 (2001).
- 458 10. J.-F. Lin *et al.*, Sound velocities of hot dense iron: Birch's law revisited. *Science* **308**, 1892-1894 (2005).
- 460 11. C. Davies, M. Pozzo, D. Gubbins, D. Alfe, Constraints from material properties on the dynamics and evolution of Earth's core. *Nat. Geosci.* **8**, 678-685 (2015).
- Q. Williams, The Thermal Conductivity of Earth's Core: A Key Geophysical Parameter's
 Constraints and Uncertainties. *Annu. Rev. Earth Planet. Sci.* 46, 47-66 (2018).
- 464 13. M. Pozzo, C. Davies, D. Gubbins, D. Alfè, Thermal and electrical conductivity of iron at Earth's core conditions. *Nature* **485**, 355-358 (2012).
- N. de Koker, G. Steinle-Neumann, V. Vlček, Electrical resistivity and thermal conductivity of liquid Fe alloys at high P and T, and heat flux in Earth's core. *Proc. Natl. Acad. Sci. USA* 109, 4070-4073 (2012).
- 469 15. K. Ohta, Y. Kuwayama, K. Hirose, K. Shimizu, Y. Ohishi, Experimental determination of the electrical resistivity of iron at Earth's core conditions. *Nature* **534**, 95-98 (2016).
- 471 16. Z. Konôpková, R. S. McWilliams, N. Gómez-Pérez, A. F. Goncharov, Direct measurement of thermal conductivity in solid iron at planetary core conditions. *Nature* **534**, 99-101 (2016).
- 473 17. S.-Y. Yue, M. Hu, Insight of the thermal conductivity of ϵ -iron at Earth's core conditions from the newly developed direct ab initio methodology. *J. Appl. Phys.* **125**, 045102 (2019).
- 475 18. L. V. Pourovskii, J. Mravlje, M. Pozzo, D. Alfè, Electronic correlations and transport in iron at Earth's core conditions. *Nat. Commun.* 11, 4105 (2020).
- M. Berrada, R. A. Secco, Review of Electrical Resistivity Measurements and Calculations of Fe
 and Fe-Alloys Relating to Planetary Cores. *Front. Earth Sci.* 9, 732289 (2021).

- W. Yong, R. A. Secco, J. A. H. Littleton, R. E. Silber, The Iron Invariance: Implications for Thermal Convection in Earth's Core. *Geophys. Res. Lett.* **46**, 11065–11070 (2019).
- 481 21. H. Gomi *et al.*, The high conductivity of iron and thermal evolution of the Earth's core. *Phys. Earth Planet. Inter.* **224**, 88-103 (2013).
- 483 22. Y. Zhang *et al.*, Reconciliation of experiments and theory on transport properties of iron and the geodynamo. *Phys. Rev. Lett.* **125**, 078501 (2020).
- 485 23. J. Xu *et al.*, Thermal conductivity and electrical resistivity of solid iron at Earth's core conditions from first-principles. *Phys. Rev. Lett.* **121**, 096601 (2018).
- 487 24. P. Olson, The new core paradox. *Science* **342**, 431-432 (2013).
- 488 25. Y. Zhang *et al.*, Transport properties of Fe-Ni-Si alloys at Earth's core conditions: Insight into the viability of thermal and compositional convection. *Earth Planet. Sci. Lett.* **553**, 116614 (2021).
- 490 26. M. Zidane *et al.*, Electrical and thermal transport properties of Fe–Ni based ternary alloys in the earth's inner core: An ab initio study. *Phys. Earth Planet. Inter.* **301**, 106465 (2020).
- F. Wagle, G. Steinle-Neumann, N. de Koker, Resistivity saturation in liquid iron–light-element alloys at conditions of planetary cores from first principles computations. *C. R. Geosci.* **351**, 154-162 (2019).
- W.-P. Hsieh *et al.*, Low thermal conductivity of iron-silicon alloys at Earth's core conditions with implications for the geodynamo. *Nat. Commun.* **11**, 3332 (2020).
- P. Driscoll, D. Bercovici, On the thermal and magnetic histories of Earth and Venus: Influences of melting, radioactivity, and conductivity. *Phys. Earth Planet. Inter.* **236**, 36-51 (2014).
- J. G. O'Rourke, D. J. Stevenson, Powering Earth's dynamo with magnesium precipitation from the core. *Nature* **529**, 387-389 (2016).
- J. Badro, J. Siebert, F. Nimmo, An early geodynamo driven by exsolution of mantle components from Earth's core. *Nature* **536**, 326-328 (2016).
- T. Mittal *et al.*, Precipitation of multiple light elements to power Earth's early dynamo. *Earth Planet. Sci. Lett.* **532**, 116030 (2020).
- Z. Du *et al.*, Insufficient Energy From MgO Exsolution to Power Early Geodynamo. *Geophys. Res. Lett.* 44, 11367-11381 (2017).
- N. Takafuji, K. Hirose, M. Mitome, Y. Bando, Solubilities of O and Si in liquid iron in equilibrium with (Mg, Fe) SiO₃ perovskite and the light elements in the core. *Geophys. Res. Lett.*32, L06313 (2005).
- 510 35. R. B. Georg, A. N. Halliday, E. A. Schauble, B. C. Reynolds, Silicon in the Earth's core. *Nature* 447, 1102-1106 (2007).
- 512 36. T. Komabayashi *et al.*, Phase relations in the system Fe–Ni–Si to 200 GPa and 3900 K and implications for Earth's core. *Earth Planet. Sci. Lett.* **512**, 83-88 (2019).
- 514 37. R. A. Fischer *et al.*, Equations of state in the Fe–FeSi system at high pressures and temperatures. 515 *J. Geophys. Res.: Solid Earth* **119**, 2810-2827 (2014).
- R. A. Fischer *et al.*, Phase relations in the Fe–FeSi system at high pressures and temperatures. *Earth. Planet. Sci. Lett.* **373**, 54-64 (2013).
- J.-F. Lin, H. P.Scott, R. A. Fischer, Phase relations of Fe-Si alloy in Earth's core. *Geophys. Res. Lett.* 36, L06306 (2009).
- 40. Z. Mao *et al.*, Sound velocities of Fe and Fe-Si alloy in the Earth's core. *Proc. Natl. Acad. Sci.* 521 USA 109, 10239-10244 (2012).
- 522 41. Y. Zhang *et al.*, Experimental constraints on light elements in the Earth's outer core. *Sci. Rep.* **6**, 523 22473 (2016).
- 42. R. A. Morrison, J. M. Jackson, W. Sturhahn, J. Zhao, T. S. Toellner, High pressure
- thermoelasticity and sound velocities of Fe-Ni-Si alloys. *Phys. Earth Planet. Inter.* **294**, 106268 (2019).
- J. Liu *et al.*, Seismic parameters of hcp-Fe alloyed with Ni and Si in the Earth's inner core. *J. Geophys. Res.: Solid Earth* 121, 610-623 (2016).

- 529 44. J. F. Lin *et al.*, Sound velocities of iron–nickel and iron–silicon alloys at high pressures. *Geophys.* 530 *Res. Lett.* **30**, 2112 (2003).
- 531 45. Y. Zhang *et al.*, Shock compression and melting of an Fe-Ni-Si alloy: implications for the temperature profile of the Earth's core and the heat flux across the core-mantle boundary. *J. Geophys. Res.: Solid Earth* **123**, 1314-1327 (2018).
- H. Ozawa, K. Hirose, K. Yonemitsu, Y. Ohishi, High-pressure melting experiments on Fe–Si alloys and implications for silicon as a light element in the core. *Earth Planet. Sci. Lett.* **456**, 47-536 54 (2016).
- H. Gomi, K. Hirose, H. Akai, Y. Fei, Electrical resistivity of substitutionally disordered hcp Fe–
 Si and Fe–Ni alloys: Chemically-induced resistivity saturation in the Earth's core. *Earth. Planet. Sci. Lett.* 451, 51-61 (2016).
- 540 48. R. E. Silber, R. A. Secco, W. Yong, J. A. Littleton, Heat flow in Earth's core from invariant electrical resistivity of Fe-Si on the melting boundary to 9 GPa: Do light elements matter? *J. Geophys. Res.: Solid Earth* **124**, 5521-5543 (2019).
- 543 49. M. Pozzo, C. Davies, D. Gubbins, D. Alfè, Thermal and electrical conductivity of solid iron and iron–silicon mixtures at Earth's core conditions. *Earth. Planet. Sci. Lett.* **393**, 159-164 (2014).
- 545 50. A. M. Dziewonski, D. L. Anderson, Preliminary reference Earth model. *Phys. Earth Planet. Inter.* **25**, 297-356 (1981).
- 51. Y. Nakajima *et al.*, Silicon-Depleted Present-Day Earth's Outer Core Revealed by Sound Velocity Measurements of Liquid Fe-Si Alloy. *J. Geophys. Res.: Solid Earth* **125**, e2020JB019399 (2020).
- 52. Q. Williams, M. H. Manghnani, R. A. Secco, S. Fu, Limitations on silicon in the outer core:
 Ultrasonic measurements at high temperatures and high dK/dP values of Fe-Ni-Si liquids at high pressures. *J. Geophys. Res.: Solid Earth* **120**, 6846-6855 (2015).
- 552 53. H. Huang *et al.*, Equation of State for Shocked Fe-8.6 wt% Si up to 240 GPa and 4,670 K. *J. Geophys. Res.: Solid Earth* 124, 8300-8312 (2019).
- 554 54. D. Ikuta, E. Ohtani, N. Hirao, Two-phase mixture of iron–nickel–silicon alloys in the Earth's inner core. *Commun. Earth Environ.* **2**, 225 (2021).
- 55. C. T. Seagle, E. Cottrell, Y. Fei, D. R. Hummer, V. B. Prakapenka, Electrical and thermal transport properties of iron and iron-silicon alloy at high pressure. *Geophys. Res. Lett.* **40**, 5377-558 5381 (2013).
- 559 56. H. Inoue, S. Suehiro, K. Ohta, K. Hirose, Y. Ohishi, Resistivity saturation of hcp Fe-Si alloys in an internally heated diamond anvil cell: A key to assessing the Earth's core conductivity. *Earth Planet. Sci. Lett.* **543**, 116357 (2020).
- 562 57. S. Anzellini, A. Dewaele, M. Mezouar, P. Loubeyre, G. Morard, Melting of iron at Earth's inner core boundary based on fast X-ray diffraction. *Science* **340**, 464-466 (2013).
- 564 58. Y. Ma *et al.*, In situ X-ray diffraction studies of iron to Earth-core conditions. *Phys. Earth Planet.* 165 *Inter.* 143, 455-467 (2004).
- 566 59. T. Komabayashi *et al.*, Phase transition boundary between fcc and hcp structures in Fe-Si alloy and its implications for terrestrial planetary cores. *Amer. Mineral.* **104**, 94-99 (2019).
- 568 60. G. Shen, V. B. Prakapenka, M. L. Rivers, S. R. Sutton, Structure of Liquid Iron at Pressures up to 58 GPa. *Phys. Rev. Lett.* **92**, 185701 (2004).
- 570 61. M. Pozzo, C. Davies, D. Gubbins, D. Alfè, Transport properties for liquid silicon-oxygen-iron mixtures at Earth's core conditions. *Phys. Rev. B* **87**, 014110 (2013).
- 572 62. D. Dobson, Geophysics: Earth's core problem. *Nature* **534**, 45-45 (2016).
- 573 63. S. Labrosse, Thermal evolution of the core with a high thermal conductivity. *Phys. Earth Planet.* 574 *Inter.* 247, 36-55 (2015).
- W.-P. Hsieh, F. Deschamps, T. Okuchi, J.-F. Lin, Effects of iron on the lattice thermal conductivity of Earth's deep mantle and implications for mantle dynamics. *Proc. Natl. Acad. Sci.*
- 577 *USA* **115**, 4099-4104 (2018).

- 578 65. Y. Okuda *et al.*, Thermal conductivity of Fe-bearing post-perovskite in the Earth's lowermost mantle. *Earth Planet. Sci. Lett.* **547**, 116466 (2020).
- 580 66. B. A. Buffett, Earth's core and the geodynamo. *Science* **288**, 2007-2012 (2000).
- 581 67. K. Schatten, S. Sofia, The Schwarzschild criterion for convection in the presence of a magnetic field. *Astrophys. Lett.* **21**, 93-96 (1981).
- 583 68. P. E. Driscoll, Z. Du, Geodynamo Conductivity Limits. *Geophys. Res. Lett.* **46**, 7982-7989 (2019).
- 585 69. B. Kennett, E. Engdahl, R. Buland, Constraints on seismic velocities in the Earth from traveltimes. *Geophys. J. Int.* **122**, 108-124 (1995).
- 587 70. B. Kennett, E. Engdahl, Traveltimes for global earthquake location and phase identification. *Geophys. J. Int.* **105**, 429-465 (1991).
- 589 71. J. C. Irving, S. Cottaar, V. Lekić, Seismically determined elastic parameters for Earth's outer core. *Sci. Adv.* 4, eaar2538 (2018).
- J. Mound, C. Davies, S. Rost, J. Aurnou, Regional stratification at the top of Earth's core due to core—mantle boundary heat flux variations. *Nat. Geosci.* **12**, 575-580 (2019).
- 593 73. G. Helffrich, S. Kaneshima, Causes and consequences of outer core stratification. *Phys. Earth Planet. Inter.* **223**, 2-7 (2013).
- J. Brodholt, J. Badro, Composition of the low seismic velocity E' layer at the top of Earth's core.
 Geophys. Res. Lett. 44, 8303-8310 (2017).
- 597 75. E. C. Thompson *et al.*, High-Pressure Geophysical Properties of Fcc Phase FeHX. *Geochem.* 598 *Geophys. Geosystems* **19**, 305-314 (2018).
- 599 76. V. Clesi *et al.*, Low hydrogen contents in the cores of terrestrial planets. *Sci. Adv.* **4**, e1701876 (2018).
- D. Alfè, M. J. Gillan, G. D. Price, Composition and temperature of the Earth's core constrained by combining ab initio calculations and seismic data. *Earth. Planet. Sci. Lett.* **195**, 91-98 (2002).
- 78. Y. Li, L. Vočadlo, D. Alfè, J. Brodholt, Carbon Partitioning Between the Earth's Inner and Outer Core. *J. Geophys. Res.: Solid Earth* **124**, 12812-12824 (2019).
- J. A. Tarduno *et al.*, Geodynamo, solar wind, and magnetopause 3.4 to 3.45 billion years ago.
 Science 327, 1238-1240 (2010).
- P. Giannozzi *et al.*, QUANTUM ESPRESSO: a modular and open-source software project for quantum simulations of materials. *J. Phys.: Condens. Matter* **21**, 395502 (2009).
- J. P. Perdew, K. Burke, M. Ernzerhof, Generalized Gradient Approximation Made Simple. *Phys. Rev. Lett.* 77, 3865-3868 (1996).
- A. van de Walle, Multicomponent multisublattice alloys, nonconfigurational entropy and other additions to the Alloy Theoretic Automated Toolkit. *Calphad* **33**, 266-278 (2009).
- 613 83. A. Zunger, S. H. Wei, L. G. Ferreira, J. E. Bernard, Special quasirandom structures. *Phys. Rev. Lett.* **65**, 353-356 (1990).
- 615 84. K. Schwarz, P. Blaha, Solid state calculations using WIEN2k. *Comput. Mater. Sci.* **28**, 259-273 (2003).
- 617 85. G. Bussi, D. Donadio, M. Parrinello, Canonical sampling through velocity rescaling. *J. Chem. Phys.* **126**, 014101 (2007).
- 619 86. H. Ebert, D. Ködderitzsch, J. Minár, Calculating condensed matter properties using the KKR-
- Green's function method—recent developments and applications. *Rep. Prog. Phys.* **74**, 096501 (2011).
- 522 87. J. Minár, Correlation effects in transition metals and their alloys studied using the fully selfconsistent KKR-based LSDA+ DMFT scheme. *J. Phys. Condens. Matter* **23**, 253201 (2011).
- 626 89. G. V. Chester, A. Thellung, The Law of Wiedemann and Franz. *Proc. Phys. Soc.* 77, 1005-1013
 627 (1961).

628	
629	Acknowledgments: We acknowledge J. Liu, C.W. Zhang, and Q. Zhang for their help in the sample
630	preparations and S.Y. Fu, L. Liang, R. Paul, and J. Smith for the synchrotron x-ray experiments at
631	Advanced Photon Source. We thank A. F. Goncharov and I. Chuvashova for the helpful discussions that
632	improved this manuscript. This work was supported by the National Natural Science Foundation of China
633	(42074098 and 41804082) and the National Science Foundation (NSF) with Grants No. EAR-1901813,
634	No. EAR-1901801 and No. EAR-1916941. R.E.C. was supported by the Carnegie Institution for Science
635	and gratefully acknowledges the Gauss Centre for Supercomputing e.V. for funding this project by
636	providing computing time on the GCS Supercomputer Supermuc-NG at Leibniz Supercomputing Centre.
637	J.M. thanks the CEDAMNF (Grant No. CZ.02.1.01/0.0/0.0/15_003/0000358), which is co-funded by the
638	ERDF as part of the Ministry of Education, Youth and Sports of Czech Republic. R.J.H. acknowledges
639	support from the National Nuclear Security Administration/Department of Energy (DE-NA0003975).
640	Electrical resistivity and x-ray diffraction measurements at high pressures and temperatures were
641	conducted at GeoSoilEnviroCARS of Advanced Photon Source (APS), Argonne National Laboratory. We
642	acknowledge the support of GeoSoilEnviroCARS (Sector 13), which is supported by the National Science
643	Foundation-Earth Sciences (EAR-1634415) and the Department of Energy, Geosciences (DE-FG02-640
644	94ER14466). This research used resources of the Advanced Photon Source, a U.S. Department of 641
645	Energy (DOE) Office of Science User Facility operated for the DOE Office of Science by Argonne
646	National Laboratory under Contract No. DE-AC02-06CH11357.
647	Author contributions: J.F.L., Y.Z., and R.E.C. designed the study. Y.Z. and M.H. prepared the cells and
648	conducted resistivity measurements. K.L., J.M., and R.E.C. conducted FPMD and DMFT computations.
649	Y.Z., N.S., J.F.L., V.B.P., E.G., and R.J.H. conducted the experiments and/or contributed to the analysis
650	of the experimental data. P.D. led the geophysical modeling calculations. Y.Z., K.L., P.D., J.F.L., R.E.C.,

and R.J.H wrote the paper. All the authors discussed the results and commented on the manuscript.

Competing interests: The authors declare no conflict of interest.

651652653

Figure legends

655 Fig. 1. Temperature-dependent electrical resistivity of hcp Fe and Fe-Si alloys at ~100 GPa. The 656 experimentally measured resistivities of hcp Fe-4.3Si (solid red squares) and Fe-9Si alloys (solid and 657 open blue squares) up to ~2500 K at pressures of 90-105 GPa show a decreasing temperature-dependence with increasing Si concentration. The resistivities of Fe-4.3Si and Fe-9Si alloys are compared with our 658 DFT/DMFT calculations, where the open diamonds represent the DFT/DMFT calculations contributed by 659 e-ph, e-e, and impurity scattering, and the semi-open diamonds represent contributions only by e-ph and 660 impurity scattering using DFT. The data for hcp Fe-4.3Si are generally consistent with the literature 661 results of hcp Fe-4Si (open black triangles) and Fe-6.5Si (open black inverted triangles) alloys at ~99 GPa 662 in an internally heated DAC (56). The open circles are for the resistivities of hcp Fe by DMFT 663 664 calculations including the contributions from e-ph and e-e scattering (23). The color dashed and dash-dot lines represent the resistivity-temperature relation in hcp Fe-4.3Si and Fe-9Si fitted using the Bloch-665 Grüneisen formula. Literature resistivity results of hcp Fe (22) and Fe-1.8Si alloy (25) are fitted using the 666 667 Bloch-Grüneisen formula (Fe: black dashed line, Fe-1.8Si: black dotted-line).

668 669

670

671

672

673

674 675

676

677

654

Fig. 2. Measured and calculated electrical resistivities of hcp Fe-4.3Si and Fe-9Si alloys up to ~3000 K at 120-136 GPa. The open and solid blue squares represent the measured resistivity of hcp Fe-9Si and the solid red squares represent the measured resistivity of hcp Fe-4.3Si. The open diamonds represent the resistivities of the Fe-Si alloys using DFT/DMFT calculations contributed by e-ph, e-e, and impurity scattering, and the semi-open diamonds represent the calculated resistivities of the Fe-Si alloys using DFT calculations contributed only by e-ph and impurity scattering. The measured high *P-T* resistivity of *hcp*-Fe (22) is also plotted for comparisons (open circles). The black dashed line represents the resistivity of hcp Fe fitted using the Bloch-Grüneisen formula. The color dashed and dash-dot lines represent the resistivity-temperature relation in hcp Fe-4.3Si and Fe-9Si fitted using the Bloch-Grüneisen formula.

678

679

680 681

682

683 684

685

686

687

688

689

690

691 692

693

694

Fig. 3. Calculated electrical resistivity (ρ_e) , thermal conductivity (κ_{el}) , and Lorenz number (L) of Fe-Si alloys in solid and liquid states at the relevant *P-T* conditions of the topmost outer core. (A) Calculated electrical resistivities of Fe-Si alloys using DFT/DMFT as a function of temperature along isochores. We assume that the Fe-Si alloys are in the solid hcp phase at temperatures below 4000 K and molten above 6000 K. Error bar has the size of ρ_{e-ss} - ρ_{e-avg} , where s = x, y, z, and ρ_{e-avg} is the average value over three directions. The anisotropy disappears for the liquid state so the standard error bar decreases. (B) Calculated thermal conductivities of Fe-Si alloys as a function of temperature along isochores. The thermal conductivity of the Fe-Si alloys increases almost linearly with increasing temperature. (C) Calculated Lorentz number (L) of the Fe-Si alloys as a function of temperature along isochores. The blue dot line represents the measured resistivity of hcp Fe-9Si and its thermal conductivity was derived using the Wiedemann-Franz relation. The calculated resistivities and thermal conductivities of liquid Fe-6.7Si by DFT are also plotted for comparisons (open squares) (14). The thermal conductivities of Fe-2Si and Fe-8Si were measured using the transient heating laser technique in LHDAC (28). Pressures (and temperatures) along the isochore in the DMFT computations for hcp Fe-9Si (54.6 bohr³ per atom) are 136 GPa (2400 K), 150 GPa (4000 K), 183 GPa (6000 K), 203 GPa (8000 K), respectively; for hcp Fe-4.3Si (55.6 bohr³ per atom) they are 122 GPa (2500 K), 135 GPa (4000 K), 169 GPa (6000 K), 188 GPa (8000

K), respectively; for hcp Fe (54.9 bohr³ per atom) they are 140 GPa (2500 K), 145 GPa (3000 K), and 149 GPa (3500 K), respectively (23).

697

698

699

700

701

702 703

704

705 706

707

708 709

710

711 712

713

714

715

695 696

> Fig. 4. Thermal stratification at the topmost outer core and energy sources for geodynamo influenced by the presence of light alloying elements. (A) Stratification thickness (z_s) at the top of the outer core as a function of the CMB heat flow (Q_{cmb}) for an adiabatic heat flow (Q_a) of ~15 TW out of the core (with the thermal conductivity of ~100 W m⁻¹ K⁻¹ for liquid Fe-9Si alloy). The thermal stratification may have a thickness in the order of a few hundred kilometers depending on the magnitude of the O_{cmb} , for example, taking the Q_{cmb} of 10-13 TW gives a thickness of 700-300 km. The presence of the stratified layer may explain the radial variation via the seismic observation in this region. The recent outer core wavespeed models AK135 (69), IASP91 (70), and KHOCQ10 (4) compared to preliminary reference Earth model (PREM) (V_p-V_{p-PREM}) vs. stratified thickness are also plotted for comparison. (B) The schematics shows that the topmost outer core is thermally stratified due to the subadiabatic heat flux across the CMB ($Q_{cmb} < Q_a$) as shown in (A). The radial convection is prevented in the stratified layer. The subadiabatic core-mantle boundary hinders thermal convection, therefore, the geodynamo is dominantly driven by compositional (chemical) convection below the stratified layer that is related to light element(s) partitioning during the inner core crystallization in (B). With the inner-core nucleation, the excess light elements (e.g., O or S) continuously release from the solid inner core to the liquid outer core at the inner-core boundary. The outer core contains ~8-10 wt.% light elements and the CMB temperature is ~4000 K.

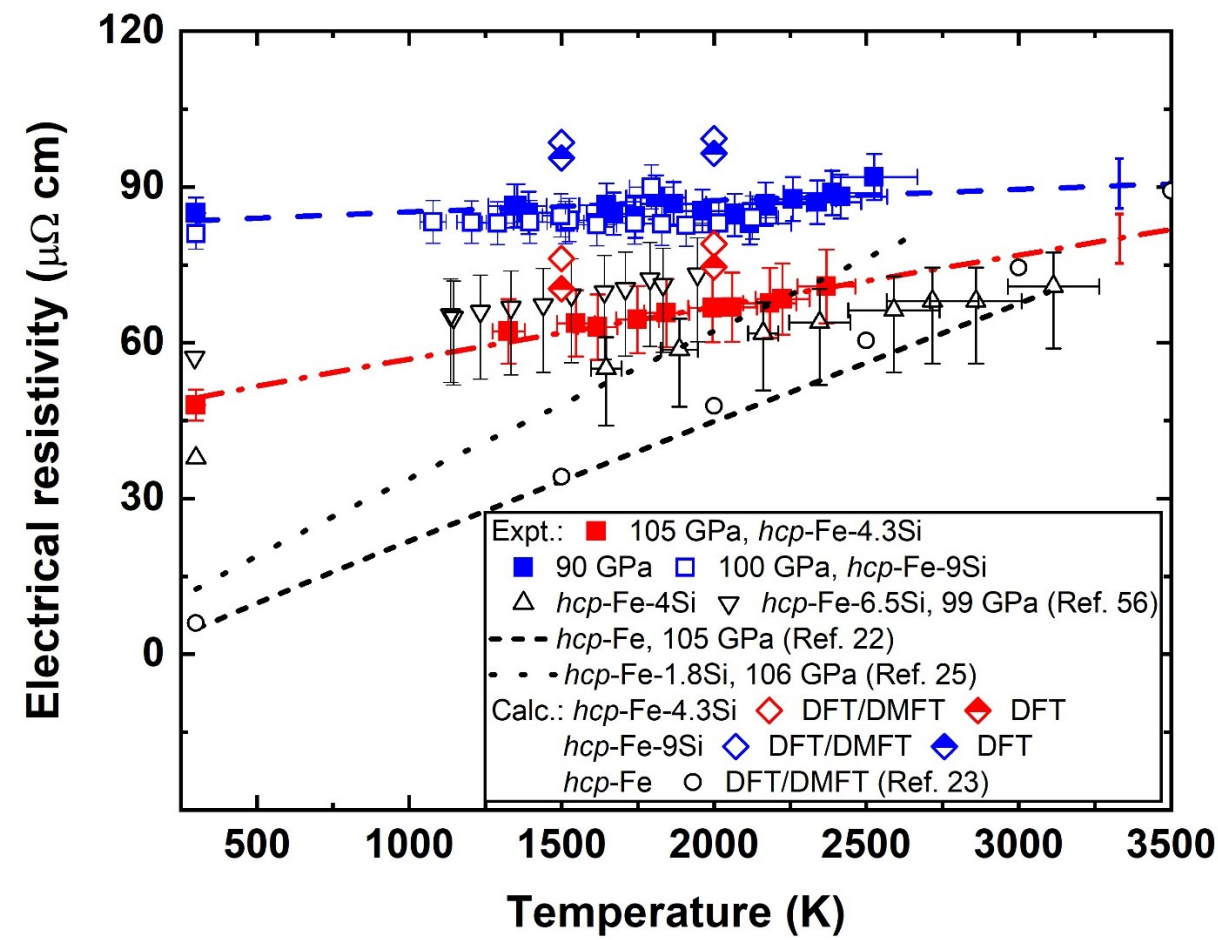


Fig. 1

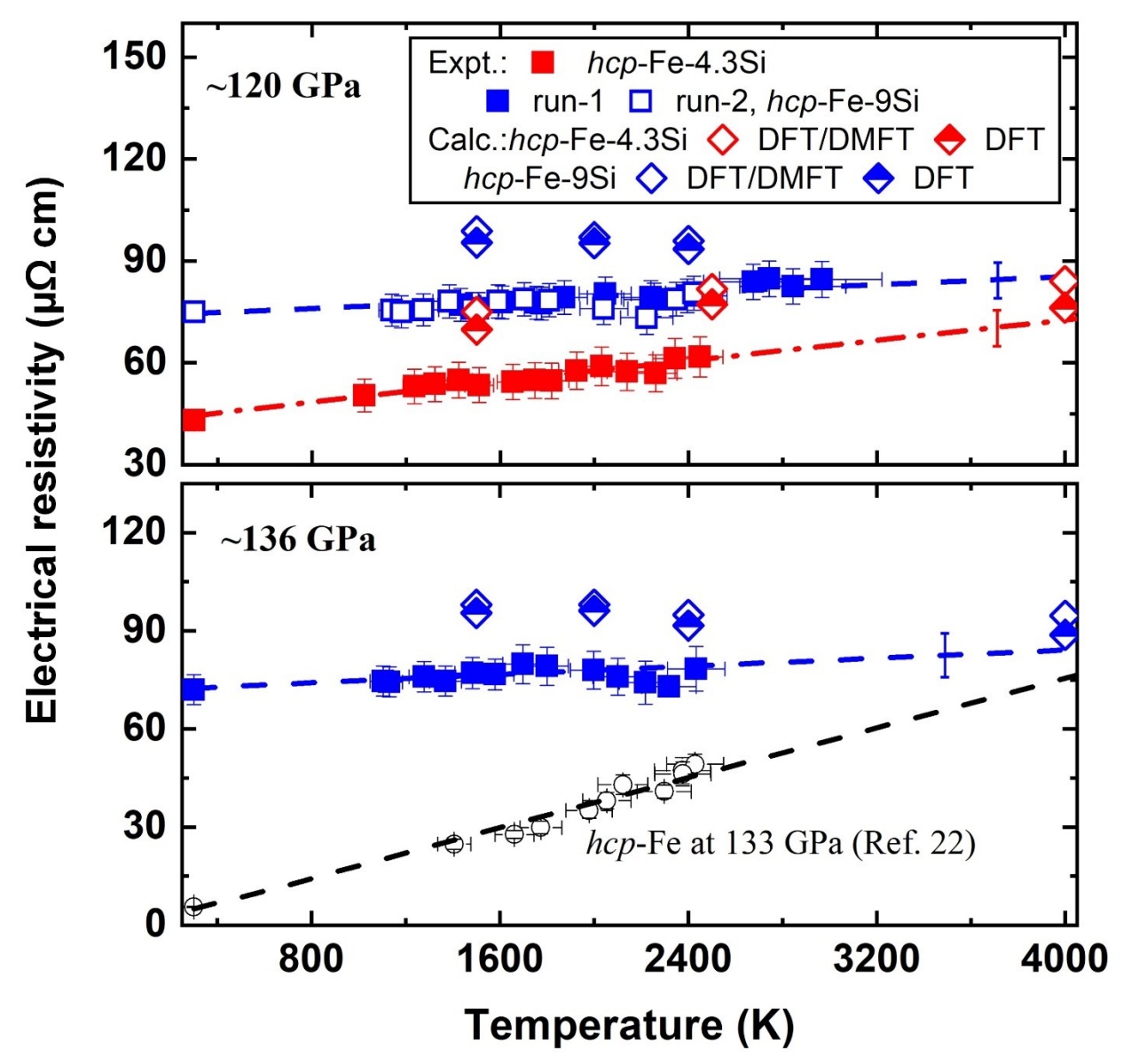


Fig. 2

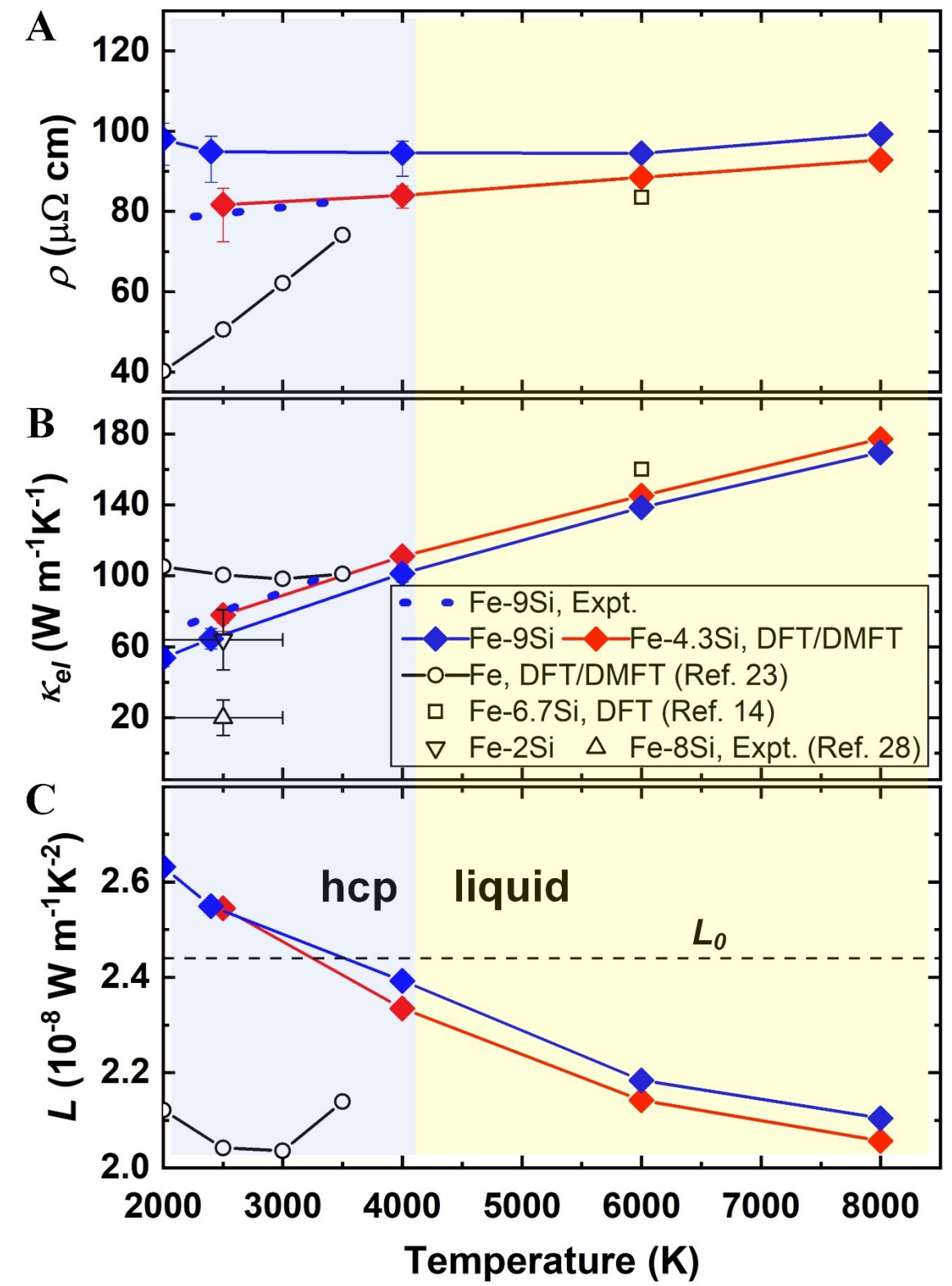
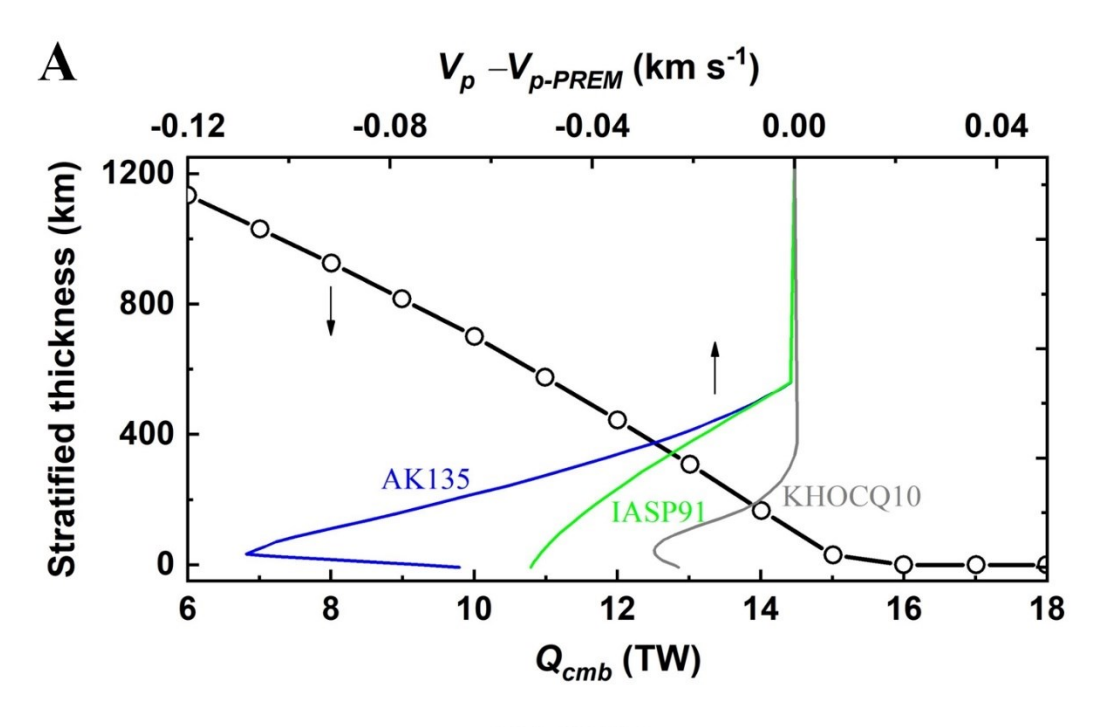
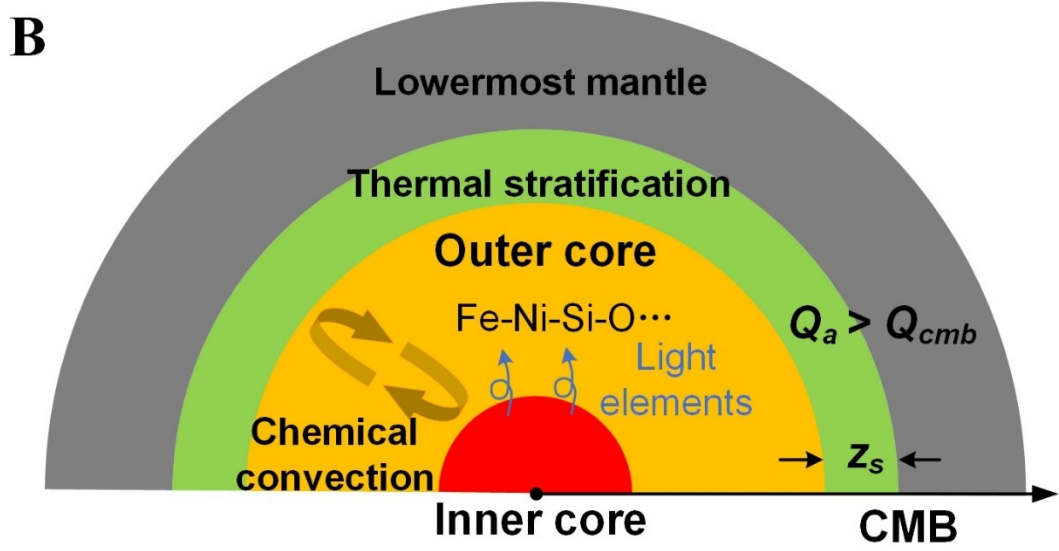


Fig. 3





723724 Fig. 4